

Supplementary Material

Simultaneous Optimization of Power Factor and Thermal Conductivity via Te and Se Double Substitution in $\text{Cu}_{12}\text{Sb}_4\text{S}_{13}$ Tetrahedrite

Umasankar Rout^{a#}, Sahil Tippireddy^{a#}, Katharina Werbach^b, Padaikathan Pambannan^c, Gerda Rogl^d, Peter Rogl^d, Ramesh Chandra Mallik^{a*}

^aThermoelectric Materials and Devices Laboratory, Department of Physics, Indian Institute of Science, Bangalore – 560012, India.

^bFaculty of Physics, University of Vienna, Boltzmanngasse 5, 1090, Vienna, Austria.

^cDepartment of Materials Engineering, Indian Institute of Science, Bangalore – 560012, India.

^dInstitute of Materials Chemistry, University of Vienna, Waehringerstrasse 42, A-1090, Wien, Austria

*Corresponding Author: rcmallik@iisc.ac.in

[#]Equal Contribution

Crystal structure and oxidation states: The Cu(1) atom at Wyckoff position 12*d*, is bonded with four S(1) atoms, which are at the corners of a regular tetrahedron. The Cu(2) atom at Wyckoff position 12*e*, is in triangular planar coordination with one S(1) and two S(2) atoms. Cu(1) possesses a mixed oxidation state of +1 and +2 while Cu(2) has an oxidation state of +1. S(1) at Wyckoff position 24*g* is coordinated tetrahedrally with two Cu(1), one Cu(2) and one Sb atom while S(2), at 2*a* Wyckoff position, is coordinated octahedrally with six Cu(2) atoms. Here, both S(1) and S(2) are in an oxidation state of -2. The Sb atom (bonded in a trigonal pyramidal fashion to S atoms) is located at Wyckoff site 8*c* with an oxidation number of +3.

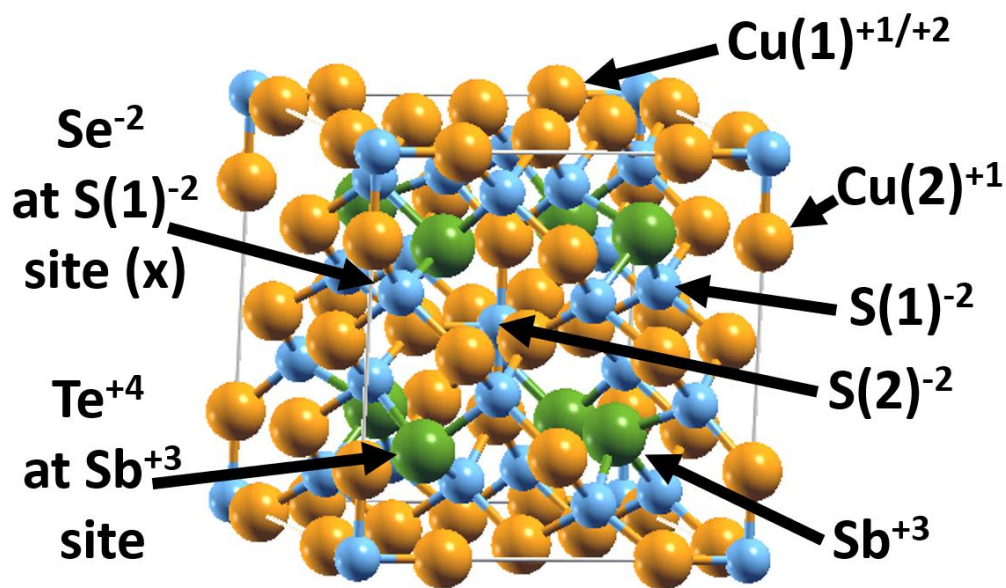


Fig. Crystal structure of $\text{Cu}_{12}\text{Sb}_4\text{S}_{13}$ tetrahedrite, showing the various Wyckoff sites and oxidation states.

Synthesis Conditions and Parameters: All the starting elements Cu, Te, S, Se (in powder form) and Sb (in shots), in highly pure form ($\sim 5\text{N}$, except Se $\sim 4\text{N}$), were taken in stoichiometric ratio, transferred into cleaned quartz ampoules and vacuum sealed at $\sim 10^{-4}$ mbar. The quartz ampoules were heated to 973 K in a Muffle furnace with a ramp time of 6 hours, soaked for 1 hour and then cooled slowly to 823 K in a ramp time of 30 hours. Following a soak time of 1 hour at 823 K, the furnace was switched off. After the furnace had cooled down to ambient temperature, the as-formed ingots were ground into powder using mortar-pestle and cold pressed. The cold pressed pellets were transferred to cleaned quartz ampoules, sealed under dynamical vacuum ($\sim 10^{-4}$ mbar) and annealed at 773 K for 48 hours. The

annealed samples were again powdered followed by sintering using a high temperature vacuum hot press at 823 K for 2 hours under a pressure of 45 MPa. The densities of all the samples were found to be ~ 95% of the theoretical density, measured using Archimedes' principle. The hot-pressed pellets were cut and shaped into cuboids ($\sim 11 \times 2 \times 2 \text{ mm}^3$) for Seebeck coefficient and electrical resistivity measurements and circular discs (diameter $\sim 12.7 \text{ mm}$ and thickness $\sim 1.3 \text{ mm}$) for thermal diffusivity measurements. A Rigaku Smart Lab X-ray diffractometer with CuK_α radiation ($\lambda = 1.54056 \text{ \AA}$) was used to obtain the powder XRD pattern of all the samples and the FullProf software was used for the Rietveld refinement of the XRD patterns. The backscattered electron (BSE) images for microstructural characterization were taken by a JEOL JXA-8530F electron probe micro analyzer along with wavelength dispersive (X-ray) spectroscopy (WDS) for obtaining the chemical composition. The vol% of the secondary phase(s) was obtained from BSE images analysis using the ImageJ software. Differential scanning calorimetry (DSC) was performed using a Mettler-Toledo DSC-822e, where all the samples were heated up to 873 K at a heating rate of 10 K per minute in an inert atmosphere. A LabRAM HR (UV) system was applied to collect the Raman Spectra of the substituted samples at room temperature with a 532 nm laser. Resonant Ultrasound Spectroscopy (RUS) was used to determine the elastic constants for the $\text{Cu}_{12}\text{Sb}_{3.9}\text{Te}_{0.1}\text{S}_{12}\text{Se}_1$ ($x = 1$) sample. This method uses the dependency of the mechanical resonances on the elastic constants to determine them with a high accuracy. The sample was placed between two piezoelectric transducers, one of which was used to excite mechanical vibrations, while the other one was used to detect the resonances. Signal acquisition was carried out with an Agilent ENA series network analyser with a signal-to-noise ratio of up to -140dBm . By iteratively minimizing the difference between at least 15 experimentally measured and theoretically predicted resonance frequencies for specific elastic parameters, the set of elastic constants with minimum deviations from the calculated frequencies was computed (within $<2 \%$ errors). Simultaneous measurement of Seebeck coefficient (S) and electrical resistivity (ρ) were performed using a Linseis LSR-3 system (373 – 673 K) in a Helium atmosphere. The thermal diffusivity (D) of all the sample were measured with a Linseis LFA 1000 (373 – 673 K) in an Argon atmosphere. The total thermal conductivity was evaluated using the formula $\kappa_T = Dd_s C_p$, where d_s is the Archimedes density of the samples and C_p taken as the Dulong-Petit specific heat capacity ($0.43 \text{ J g}^{-1} \text{ K}^{-1}$).

Theoretical Calculation Details: For a qualitative understanding of the influence of Te and Se substitution on the bandstructure of tetrahedrite, theoretical calculations (DFT) were performed for two compositions: 1) only Te substituted: $\text{Cu}_{12}\text{Sb}_{3.5}\text{Te}_{0.5}\text{S}_{13}$ and 2) Te and Se double substituted: $\text{Cu}_{12}\text{Sb}_{3.5}\text{Te}_{0.5}\text{S}_{12.5}\text{Se}_{0.5}$. DFT calculations were performed using the Quantum ESPRESSO package[1] taking the generalized gradient approximation (GGA) proposed by Perdew, Burke, and Ernzerhof[2] for the exchange-correlation functional. The wavefunctions were described using plane-wave basis sets with an energy cut-off of 475 eV. A $7 \times 7 \times 7$ Monkhorst-Pack k-point grid was taken for the scf and relaxation calculations. The band structure calculations were performed along the high-symmetry k-point directions in the reciprocal space. A body-centered cubic (BCC) structure with 58 atoms in the conventional unit cell and a lattice parameter of 10.33 Å was considered, with Te substituted at the Sb 8c and Se at the S(1) 24g Wyckoff sites, respectively. A force threshold of 0.01 eV/Å was used for the structure relaxation. The spin polarized DFT calculations were also performed for the compositions and it was found that Te/Se does not lead to any polarization of the band structure.

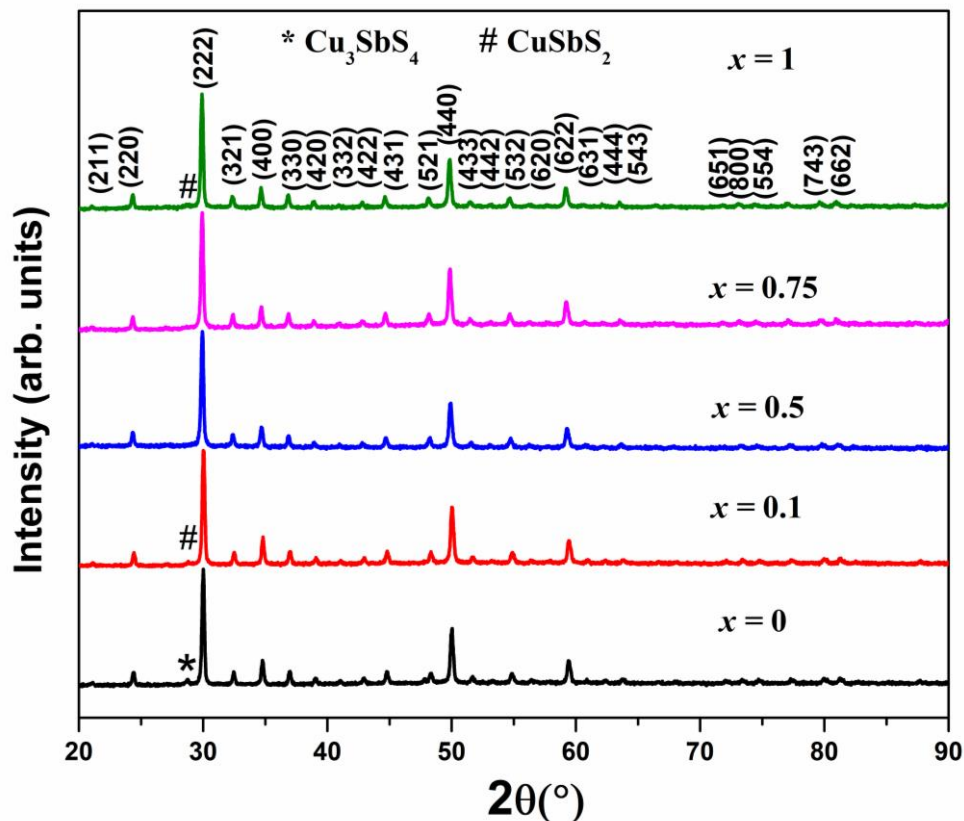


Fig. S1. X-ray diffraction (XRD) patterns of the substituted $\text{Cu}_{12}\text{Sb}_{3.9}\text{Te}_{0.1}\text{S}_{13-x}\text{Se}_x$ ($x = 0, 0.1, 0.5, 0.75$ and 1) samples indexed with ICDD PDF # 00-024-1318 and marked with secondary phases.

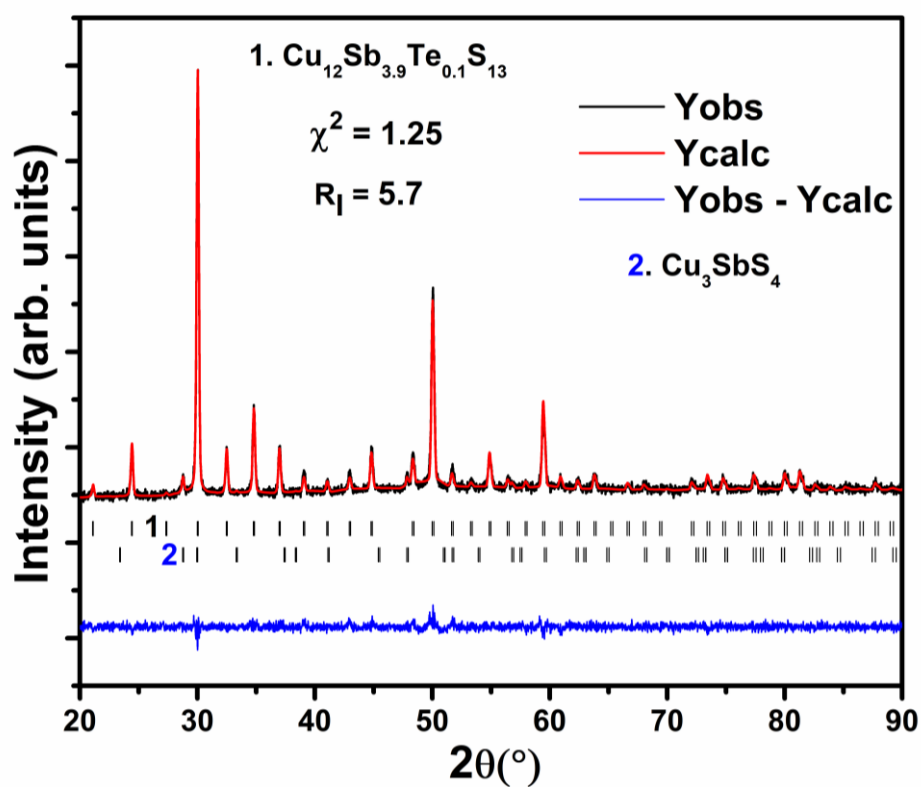


Fig. S2. Refined XRD pattern for $\text{Cu}_{12}\text{Sb}_{3.9}\text{Te}_{0.1}\text{S}_{13}$

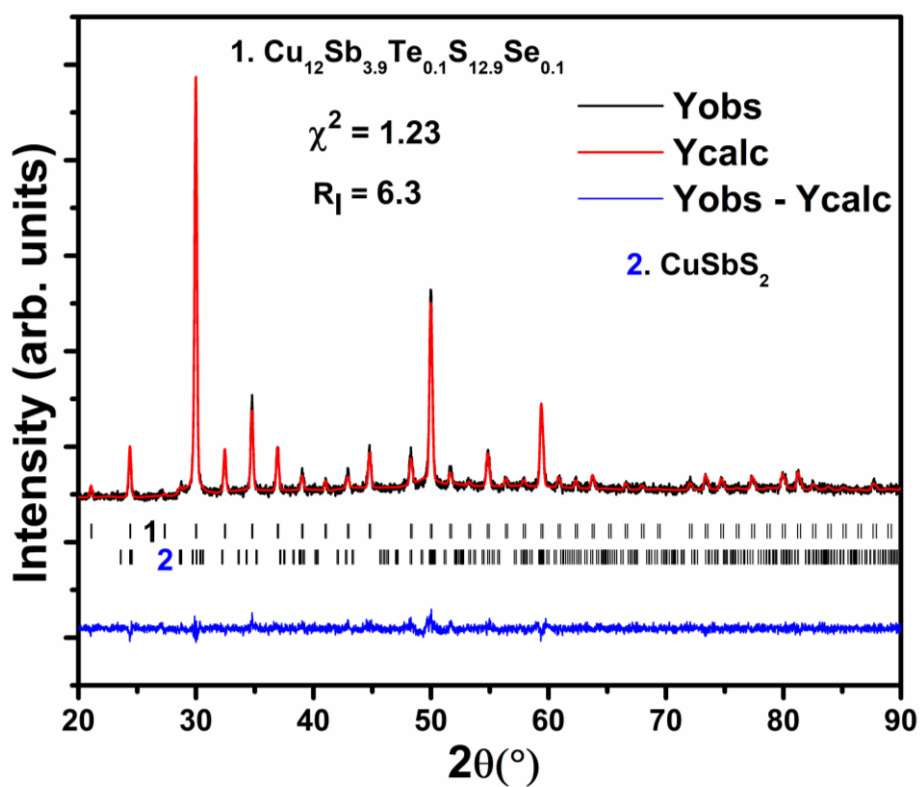


Fig. S3. Refined XRD pattern for $\text{Cu}_{12}\text{Sb}_{3.9}\text{Te}_{0.1}\text{S}_{12.9}\text{Se}_{0.1}$

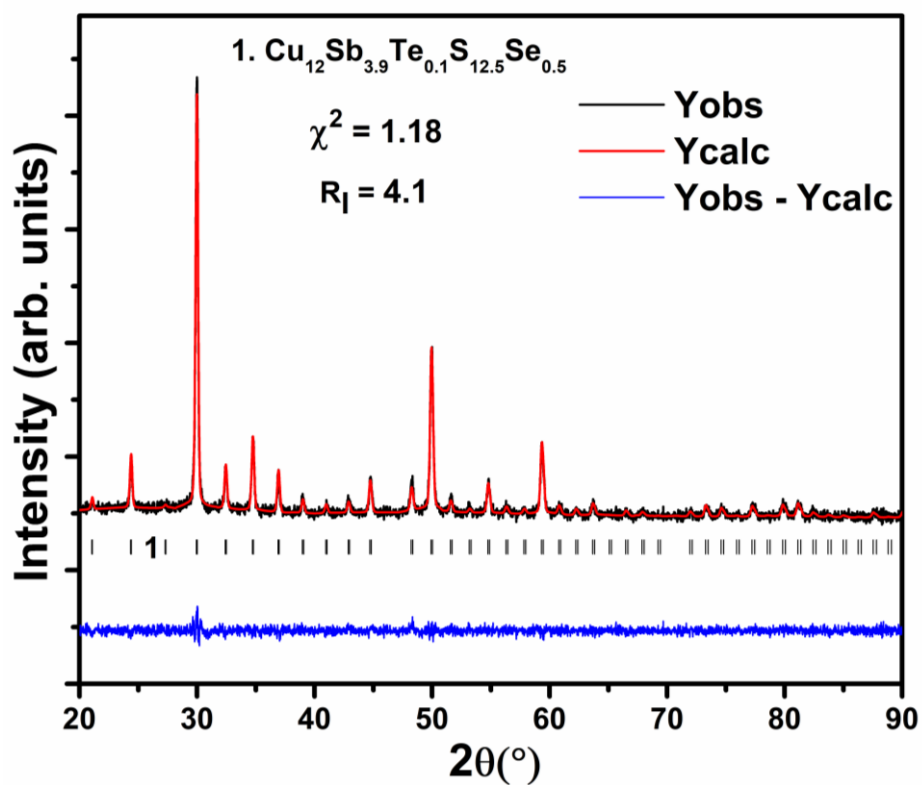


Fig. S4. Refined XRD pattern for $\text{Cu}_{12}\text{Sb}_{3.9}\text{Te}_{0.1}\text{S}_{12.5}\text{Se}_{0.5}$

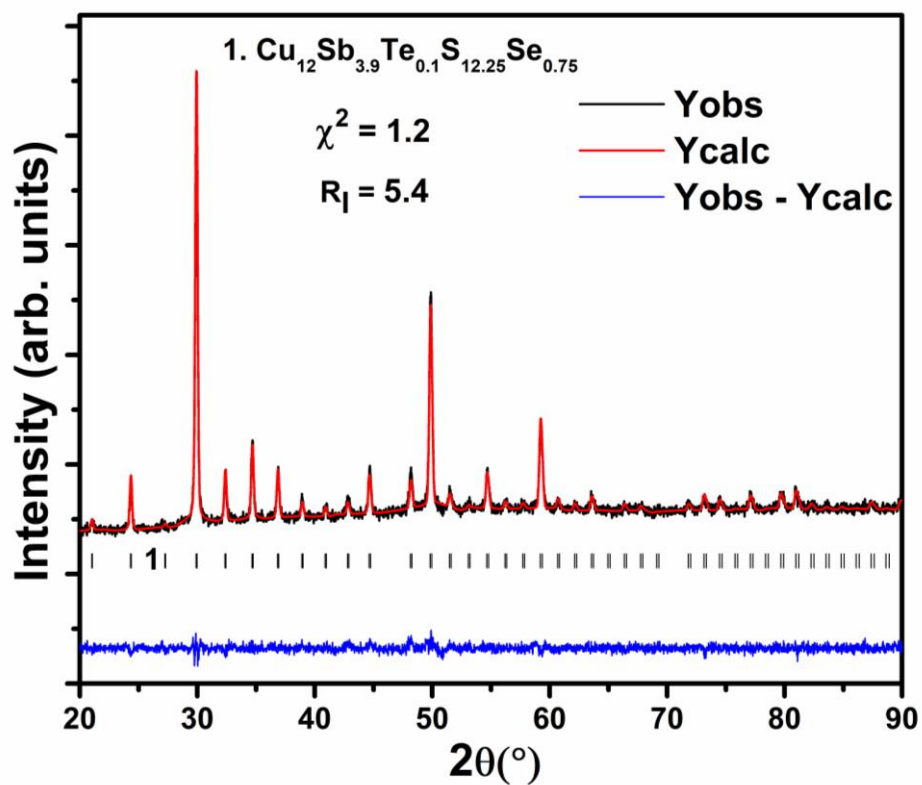


Fig. S5. Refined XRD pattern for $\text{Cu}_{12}\text{Sb}_{3.9}\text{Te}_{0.1}\text{S}_{12.25}\text{Se}_{0.75}$

Table T1: Lattice parameter as a function of Se concentration in $\text{Cu}_{12}\text{Sb}_{3.9}\text{Te}_{0.1}\text{S}_{13-x}\text{Se}_x$ ($x = 0, 0.1, 0.5, 0.75$ and 1)

Sample	Lattice Parameter
$\text{Cu}_{12}\text{Sb}_{3.9}\text{Te}_{0.1}\text{S}_{13}$ ($x = 0$)	10.310(1)
$\text{Cu}_{12}\text{Sb}_{3.9}\text{Te}_{0.1}\text{S}_{12.9}\text{Se}_{0.1}$ ($x = 0.1$)	10.316(7)
$\text{Cu}_{12}\text{Sb}_{3.9}\text{Te}_{0.1}\text{S}_{12.5}\text{Se}_{0.5}$ ($x = 0.5$)	10.328(6)
$\text{Cu}_{12}\text{Sb}_{3.9}\text{Te}_{0.1}\text{S}_{12.25}\text{Se}_{0.75}$ ($x = 0.75$)	10.342(8)
$\text{Cu}_{12}\text{Sb}_{3.9}\text{Te}_{0.1}\text{S}_{12}\text{Se}_1$ ($x = 1$)	10.354(1)

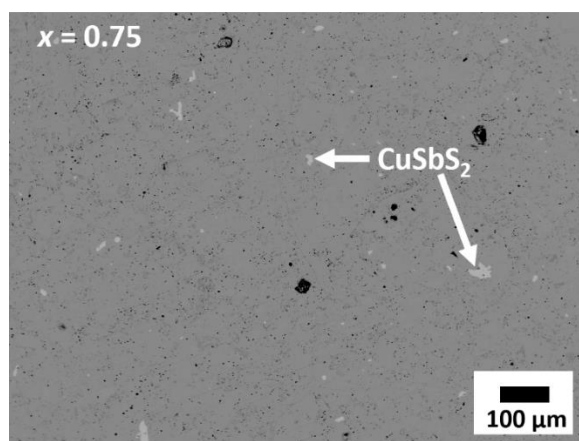


Fig. S6. Backscattered image (BSE) for $\text{Cu}_{12}\text{Sb}_{3.9}\text{Te}_{0.1}\text{S}_{12.25}\text{Se}_{0.75}$ ($x = 0.75$) sample marked with secondary phase.

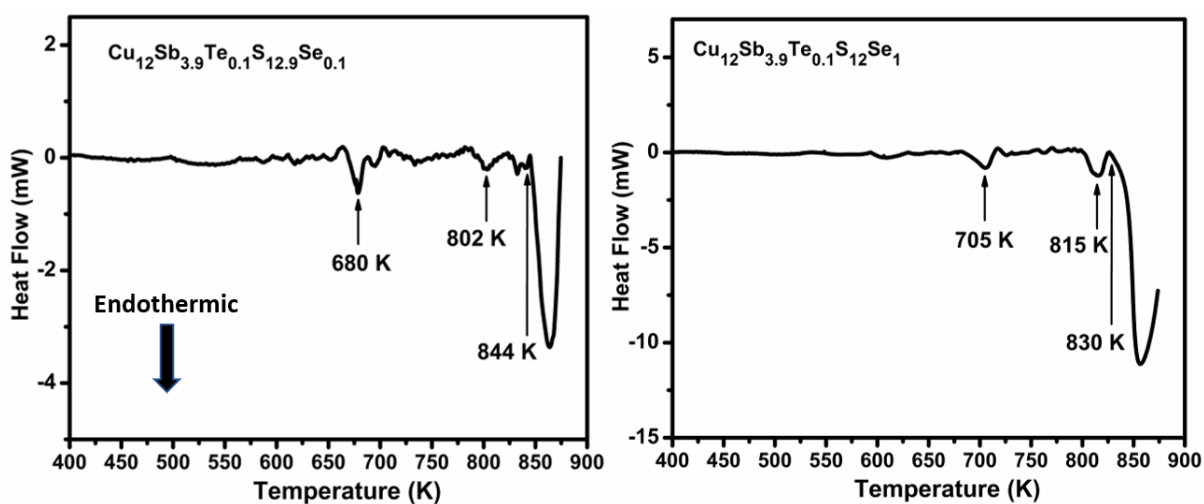


Fig. S7. Differential scanning calorimetry (DSC) traces of the double substituted $\text{Cu}_{12}\text{Sb}_{3.9}\text{Te}_{0.1}\text{S}_{13-x}\text{Se}_x$ ($x = 0.1, 0.5$ and 1) samples marked with the major endothermic peaks.

All samples were observed to be thermally stable from room temperature to ~680 K, with no endo/exothermic peaks up to this temperature. An endothermic peak around 680 – 705 K was exhibited by the samples due to Sulphur volatilization in the samples[3,4], followed by another endothermic peak at around 802 – 815 K, which can be attributed to the reorganization of the crystal structure and the subsequent onset of phase transformation[3,4]. Finally, a sharp endothermic peak at 830 – 845 K was observed in the samples, corresponding to the decomposition of the tetrahedrite phase into Cu_2S and CuSbS_2 phases[4–6]. The decomposition temperatures are higher compared to those of only Te substituted samples[3] (720 – 740 K) of the literature; and in fact, also higher compared to those of transition metal[5] (~810 K) and Al substituted[4] (~770 K) samples.

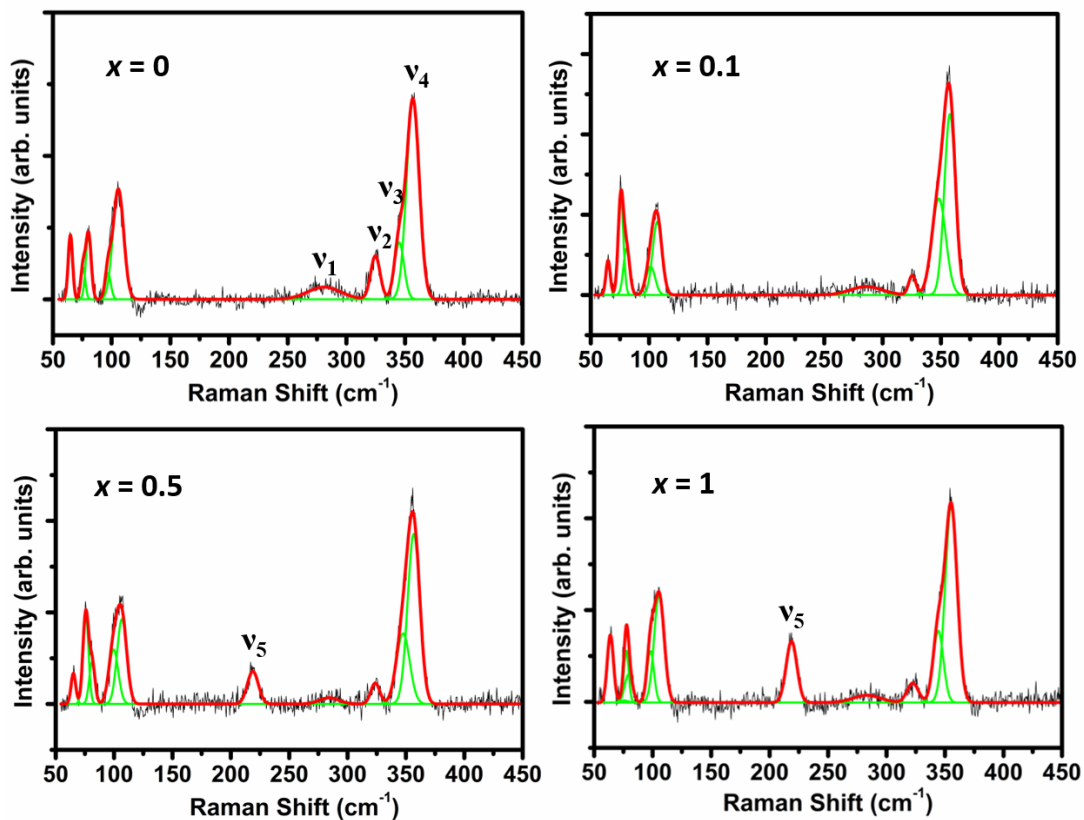


Fig. S8. Deconvoluted Raman spectra of $\text{Cu}_{12}\text{Sb}_{3.9}\text{Te}_{0.1}\text{S}_{13-x}\text{Se}_x$ ($x = 0, 0.1, 0.5$ and 1) samples

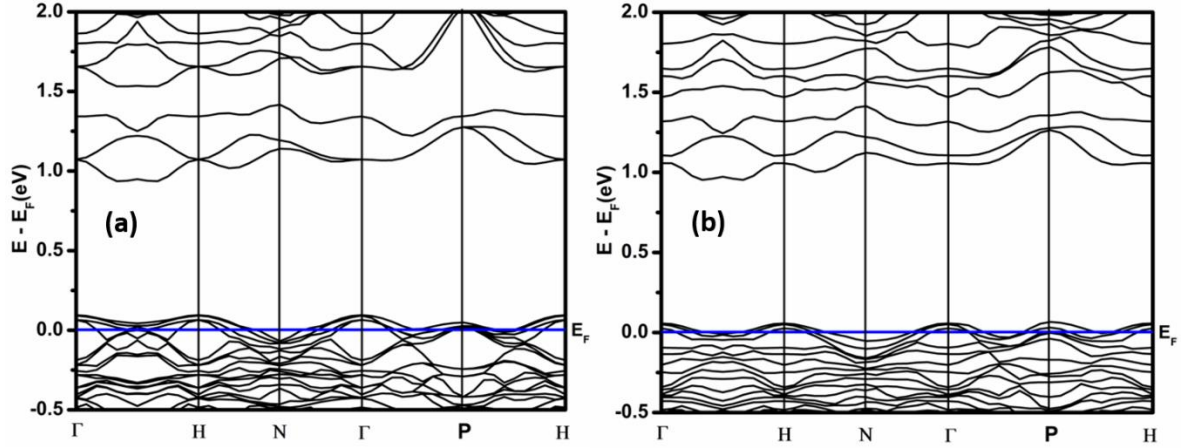


Fig. S9. Bandstructures of (a) $\text{Cu}_{12}\text{Sb}_{3.5}\text{Te}_{0.5}\text{S}_{13}$ and (b) $\text{Cu}_{12}\text{Sb}_{3.5}\text{Te}_{0.5}\text{S}_{12.5}\text{Se}_{0.5}$.

Initially for only Te substitution in tetrahedrite ($\text{Cu}_{12}\text{Sb}_{3.5}\text{Te}_{0.5}\text{S}_{13}$), the Fermi level (E_F) is shifted towards the bandgap (compared to pristine $\text{Cu}_{12}\text{Sb}_4\text{S}_{13}$ [5]) due to charge carrier (holes) compensation caused by Te^{+4} at the Sb^{+3} site. But with additional introduction of Se in $\text{Cu}_{12}\text{Sb}_{3.5}\text{Te}_{0.5}\text{S}_{12.5}\text{Se}_{0.5}$, the lighter hole bands below the Fermi level move up in energy and converge with the top most bands. A similar bandstructure modification was also seen in other Se substituted compositions in the literature [9,10]. Consequently, the charge carriers in double substituted $\text{Cu}_{12}\text{Sb}_{3.5}\text{Te}_{0.5}\text{S}_{12.5}\text{Se}_{0.5}$ now have additional conduction channels with lower effective mass, exhibiting relatively higher charge carrier mobility as compared to that of only Te substituted $\text{Cu}_{12}\text{Sb}_{3.5}\text{Te}_{0.5}\text{S}_{13}$. Additionally, the DOS near E_F in $\text{Cu}_{12}\text{Sb}_{3.5}\text{Te}_{0.5}\text{S}_{12.5}\text{Se}_{0.5}$ is also enlarged due to band convergence as compared to $\text{Cu}_{12}\text{Sb}_{3.5}\text{Te}_{0.5}\text{S}_{13}$ (which can be seen in Fig. 3 of the main manuscript). Although, we have not performed DFT calculations for higher concentrations of Se, we can infer a fairly accurate picture of the bandstructure (with higher Se content) based on the similarities of bandstructure, PDOS and substitution strategy (Se at S1 site) between this work, and that of previous Se substituted tetrahedrite reports in the literature [9,10]. Both Lu et al. [9] (for singly substituted Se tetrahedrite) and Tippireddy et al. [10] (for Zn and Se double substituted tetrahedrite), have reported that an increase in Se content is accompanied with an increase in the light hole bands near E_F . Hence, the band-edge should be modified with an increase in Se content, with the charge carriers having access to additional carrier pockets with higher band dispersion (or lower average effective mass). However, since Se is isovalent with S, the total number of charge carriers occupying the bands is expected to remain similar. The only modification is that the charge carriers attain a lower average effective mass and consequently, a higher average charge carrier mobility, with increase in Se content [9,10]. Physically, this stems from an increased overlap of the Se orbitals with those of the

adjacent atoms, increasing the bond covalency, and thereby reducing the average effective mass [10].

Electrical Resistivity: Detailed Explanation

All the samples showed an increase in electrical resistivity with temperature indicating that the samples are degenerate semiconductors in nature. Initially, for the only Te substituted sample, $\text{Cu}_{12}\text{Sb}_{3.9}\text{Te}_{0.1}\text{S}_{13}$, ρ lies in the range: 0.0128 – 0.0169 m Ω m across the measured temperature range, which is higher than that of pristine $\text{Cu}_{12}\text{Sb}_4\text{S}_{13}$ (0.010 – 0.012 m Ω m[7]). This occurs primarily due to the substitution of Te^{+4} at the Sb^{+3} site, as Se^{-2} is isovalent with S^{-2} and hence does not take part in charge carrier compensation. Substitution of Te^{+4} introduces electrons into the system which compensates holes and consequently reduces the net charge carrier concentration with an increase in the electrical resistivity. The reduction in the charge carrier concentration (n) was also confirmed from DFT calculations where the Fermi level for only Te substituted composition was lifted towards the bandgap, as compared to the pristine tetrahedrite ($\text{Cu}_{12}\text{Sb}_4\text{S}_{13}$) due to charge carrier (holes) compensation. The values of the electrical resistivity of the only Te substituted sample ($\text{Cu}_{12}\text{Sb}_{3.9}\text{Te}_{0.1}\text{S}_{13}$) are within 8-10% compared to that of the same composition in the literature.[8] The slight variation could be due to changes in stoichiometry, synthesis conditions, instrumental errors and contribution from the secondary phase(s). Since the charge carrier concentration (n) should be similar in all the double substituted samples (as Se is isovalent with S), the electrical resistivity (ρ) with varying Se content should mainly be a function of charge carrier mobility (μ) according to the following equation:

$$\rho = \frac{1}{ne\mu} = \frac{m_b^*}{ne^2\tau} \quad (\text{E1})$$

where we have used $\mu = e\tau/m_b^*$, with e , τ and m_b^* denoting the electronic charge, carrier relaxation time and band effective mass, respectively. From Equation E1, the electrical resistivity is directly proportional to the band effective mass which can be related to the curvature of the band (d^2E/dk^2) near E_F by:

$$m_b^* = \frac{\hbar^2}{d^2E/dk^2} \quad (\text{E2})$$

where \hbar is the reduced Plank's constant. Equation E1 also indicates that ρ is inversely proportional to the carrier relaxation time (τ), which is limited by the different scattering mechanisms in the system. Hence, the relative weightage of m_b^* (numerator) and τ

(denominator) will determine the overall net electrical resistivity of the samples. With Se addition in $\text{Cu}_{12}\text{Sb}_{3.9}\text{Te}_{0.1}\text{S}_{12.9}\text{Se}_{0.1}$ having low Se content (0.34 at%), the average band effective mass (m_b^*) reduces following from a higher dispersion (or curvature) of the additional light-hole bands near E_F due to hybridization of Se 4p states with that of host atoms near the Fermi level. Consequently, the average charge carrier mobility (μ) increases following from Equation E1 and hence the electrical resistivity was reduced compared to that of the only Te substituted ($x = 0$) sample. However, with further increase in the Se content in $x = 0.5$ sample, $\text{Cu}_{12}\text{Sb}_{3.9}\text{Te}_{0.1}\text{S}_{12.5}\text{Se}_{0.5}$ (1.72 at%), the electrical resistivity increased, compared to both $x = 0$ ($\text{Cu}_{12}\text{Sb}_{3.9}\text{Te}_{0.1}\text{S}_{13}$) and $x = 0.1$ ($\text{Cu}_{12}\text{Sb}_{3.9}\text{Te}_{0.1}\text{S}_{12.9}\text{Se}_{0.1}$). The double substitution with Te and a higher Se content ($x > 0.1$) can lead to point defects, including vacancies and interstitials, that may contribute to additional charge carrier scattering and a lowering of carrier relaxation time (τ). This was also seen in previous reports with Se substitution in tetrahedrite [9,10]. Therefore, the reduction of the denominator (τ) in Equation E1 dominates over the change in m_b^* (numerator), resulting in an overall reduced net charge carrier mobility (compared to $x < 0.1$). As a result, a relatively higher electrical resistivity for the $x = 0.5$ ($\text{Cu}_{12}\text{Sb}_{3.9}\text{Te}_{0.1}\text{S}_{12.5}\text{Se}_{0.5}$) sample was observed. With further increase in Se content (2.58 at%) in $\text{Cu}_{12}\text{Sb}_{3.9}\text{Te}_{0.1}\text{S}_{12.25}\text{Se}_{0.75}$ ($x = 0.75$), however, the electrical resistivity further dropped (compared to the $x = 0.5$ sample). The reason is again a trade-off between charge carrier scattering caused by defects (limiting the τ term) and the improved band effective mass (m_b^*) caused by the additional light hole bands near E_F (due to Se 4p states). The relatively high (2.58 at%) Se concentration in $\text{Cu}_{12}\text{Sb}_{3.9}\text{Te}_{0.1}\text{S}_{12.25}\text{Se}_{0.75}$ leads to a greater number of light hole bands near E_F resulting in an even lower average band effective mass, which dominates over the scattering caused by the defects. As a result, the reduction in the numerator (m_b^*) now dominates over the denominator (τ) in Equation E1, resulting in a higher net average charge carrier mobility with a reduction in the electrical resistivity for $x = 0.75$ and 1 samples. Another main reason for the observed trend of ρ with Se content (x) can be inferred from the EPMA results, which showed that the samples contained the secondary phase of CuSbS_2 (chalcostibite) with Se partially substituted at the S site, forming the $\text{CuSbS}_{2-y}\text{Se}_y$ phase. The partial substitution of Se in $\text{CuSbS}_{2-y}\text{Se}_y$ modifies the bandstructure of chalcostibite and reduces the bandgap[11]. This is accompanied by a significant change in the electrical resistivity of CuSbS_2 (no Se at S site) from non-degenerate behaviour to a degenerate one in CuSbSe_2 (complete substitution of Se at S site) with a drop of ~70 % in ρ values [12,13]. For the $x = 1$ sample, this $\text{CuSbS}_{2-y}\text{Se}_y$ secondary phase was high (~2.5 vol%) which may contribute to its

overall low electrical resistivity and hence the $x = 1$ sample showed considerably low ρ values. On the other hand, the $x = 0.5$ sample contained the least and almost negligible amount of $\text{CuSbS}_{2-y}\text{Se}_y$ secondary phase (~ 0.1 vol%), and therefore was not affected by the lower electrical resistivity of the $\text{CuSbS}_{2-y}\text{Se}_y$ phase. As a result, it showed a relatively higher electrical resistivity compared to other samples. It should be noted that Hall measurements were attempted to evaluate the charge carrier concentration as well as to confirm the charge carrier compensation and charge carrier mobility analysis. But we could not obtain coherent and conclusive results due to low and arbitrary Hall coefficients, which was also observed in many of the previous reports[4,5,10,14].

Seebeck Coefficient: Detailed Explanation

It was observed that except for the $x = 0.5$ sample, all samples showed nearly invariant Seebeck coefficients with varying Se content. The S values of these samples lay between $\sim 92 - 138$ $\mu\text{V/K}$ across the measured temperature range, which is $\sim 10 - 20\%$ higher than the pristine ($\text{Cu}_{12}\text{Sb}_4\text{S}_{13}$) case [7], due to hole compensation by Te^{+4} at the Sb^{+3} site and a consequent decrease in the charge carrier concentration. The near invariance of the Seebeck coefficient in these samples can be understood from Mott's formula given below:

$$S = \frac{\pi^2}{3} k_B^2 T \left[\frac{1}{n} \frac{dn}{dE} + \frac{1}{\mu} \frac{d\mu}{dE} \right]_{E=E_F} \quad (\text{E3})$$

where k_B , E , n , μ , E_F and T represent the Boltzmann constant, energy, charge carrier concentration, charge carrier mobility, Fermi energy and absolute temperature, respectively. The dn/dE term on the right-hand side of Equation E3 corresponds to the density of states near E_F and $d\mu/dE$ term represents the change of charge carrier mobility μ with energy, which should be invariant with increasing x [9,10,15]. From DFT calculations and electrical resistivity results, it was inferred that an increasing Se concentration increases both the DOS near E_F and the average charge carrier mobility (or decrease of $1/\mu$ factor), due to additional Se 4p states near E_F . Hence, the two terms: dn/dE and $1/\mu$ are balanced, assuming that the charge carrier concentration remains the same (since Te concentration is almost the same in all the samples). As a result, the overall Seebeck coefficient was found to be almost invariant with varying Se concentration, at the same time, maintaining relatively high values. A similar trend was also observed in previous studies with Se single and double substituted compounds[9,10,15]. However, for the $x = 0.5$ sample ($\text{Cu}_{12}\text{Sb}_{3.9}\text{Te}_{0.1}\text{S}_{12.5}\text{Se}_{0.5}$), apart from an increase in the DOS near E_F (or dn/dE term), the charge carrier mobility was, in fact, not much enhanced, hence resulting in a relatively higher $1/\mu$ factor. This was due to the charge carrier scattering by

defects dominating over a reduced m_b^* (Equation E1), as observed in the electrical resistivity results and explained in the previous section. Consequently, the $x = 0.5$ sample exhibited a relatively higher Seebeck coefficient ($\sim 100 - 150 \mu\text{V/K}$ across the measured temperature range), compared to other samples. In addition, the Se partially substituted $\text{CuSbS}_{2-y}\text{Se}_y$ secondary phase may also play a role in influencing the overall Seebeck coefficient trend as a function of x . As mentioned previously, the partial substitution of Se at the S site in $\text{CuSbS}_{2-y}\text{Se}_y$ reduces the bandgap and modifies the system from a non-degenerate semiconductor to a degenerate one, accompanied by a significant reduction of Seebeck coefficient [11–13]. Therefore, here again, the negligible amount of $\text{CuSbS}_{2-y}\text{Se}_y$ in the $x = 0.5$ sample, did not reduce its overall S values, hence, resulting in a relatively higher Seebeck coefficient, compared to other samples (having higher content of $\text{CuSbS}_{2-y}\text{Se}_y$). In general, the S values of all the samples were $\sim 10\text{-}25\%$ higher than those of the pristine $\text{Cu}_{12}\text{Sb}_4\text{S}_{13}$, mainly due to an enhancement of DOS near E_F .

Thermal Conductivity: Detailed Explanation

The electronic thermal conductivity (κ_e) was derived from the Wiedemann-Franz relation:

$$\kappa_e = L\sigma T \quad (\text{E4})$$

where T is the temperature and L is the temperature dependent Lorenz number. L was evaluated from the Seebeck coefficient values assuming a single parabolic model and acoustic phonon scattering via:

$$L = \left(\frac{k_B}{e}\right)^2 \left[\frac{3F_0(\eta)F_2(\eta) - 4F_1^2(\eta)}{F_0^2(\eta)} \right] \quad (\text{E5})$$

where k_B , e , and F_n are the Boltzmann constant, electronic charge and Fermi integrals of order n , respectively. η is the reduced Fermi energy, which is derived from Seebeck coefficient values at each temperature via:

$$S = \pm \frac{k_B}{e} \left(2 \frac{F_1(\eta)}{F_0(\eta)} - \eta \right) \quad (\text{E6})$$

The lattice thermal conductivity (κ_L) of all the samples was obtained from the difference of total and electronic thermal conductivities.

The electronic thermal conductivity, κ_e , increased with increase in temperature and the trend of κ_e as a function of substituent concentration follows the electrical resistivity trend, based on the charge carrier compensation and charge carrier scattering mechanisms, as explained

previously. The total thermal conductivity, κ_T , in the double substituted samples, as a function of temperature, first increased till 475 K, flattened (475 – 675 K) and then decreased for temperatures > 675 K. This is because initially till ~450-475 K, both κ_e and κ_L components increased with increase in temperature, resulting in the increase in total thermal conductivity. But after 475-500 K, the κ_L component decreased with increase in temperature due to the onset of dominant Umklapp (phonon-phonon) scattering at higher temperatures, which compensated the increase in κ_e component. As a result, the total thermal conductivity remained almost constant in the temperature range: 475-675 K. But at higher temperatures (>650-675 K), the further decrease in κ_L dominated over the increase in κ_e contribution. Consequently, the total thermal conductivity decreased with further increase in temperature. The lattice thermal conductivity of the double substituted samples was observed to be quite low due to the reasons highlighted in the manuscript. However, the trend of the lattice thermal conductivity with x , especially the relatively lower κ_L of the $x = 0.5$ sample, can again be understood based on the vol% of the CuSbS_2 secondary phase in the samples. The thermal conductivity of CuSbS_2 (chalcostibite) at 300 K is ~40% higher than that of tetrahedrite[16], which is mostly dominated by the lattice contribution[16]. In addition, the partial substitution of Se at the S site in chalcostibite forming the $\text{CuSbS}_{2-y}\text{Se}_y$ phase (as seen in EPMA), will also enhance its electronic part of thermal conductivity due to the enhancement of electrical conductivity (as explained previously). Hence, the overall thermal conductivity of the samples (including the lattice contribution), which contain relatively higher vol% of $\text{CuSbS}_{2-y}\text{Se}_y$ secondary phase (i.e. $x = 0, 0.1$ and 0.75 sample), was observed to be relatively higher. But in the case of $x = 0.5$ sample, there is negligible amount of $\text{CuSbS}_{2-y}\text{Se}_y$ secondary phase, which, therefore, does not affect its overall thermal (including lattice) conductivity. Consequently, the $x = 0.5$ sample showed a lower lattice thermal conductivity. However, although the $x = 1$ sample contains a relatively higher vol% of $\text{CuSbS}_{2-y}\text{Se}_y$ secondary phase, it also exhibits a very low lattice thermal conductivity. This is due to a higher percentage of Se content in the $x = 1$ sample, which leads to a higher local chemical disorder, Sb-S bond softening and higher S-Se mass difference phonon scattering, which dominate over the higher thermal conductivity of the $\text{CuSbS}_{2-y}\text{Se}_y$ secondary phase. As a result, the $x = 1$ sample also exhibited a low lattice thermal conductivity.

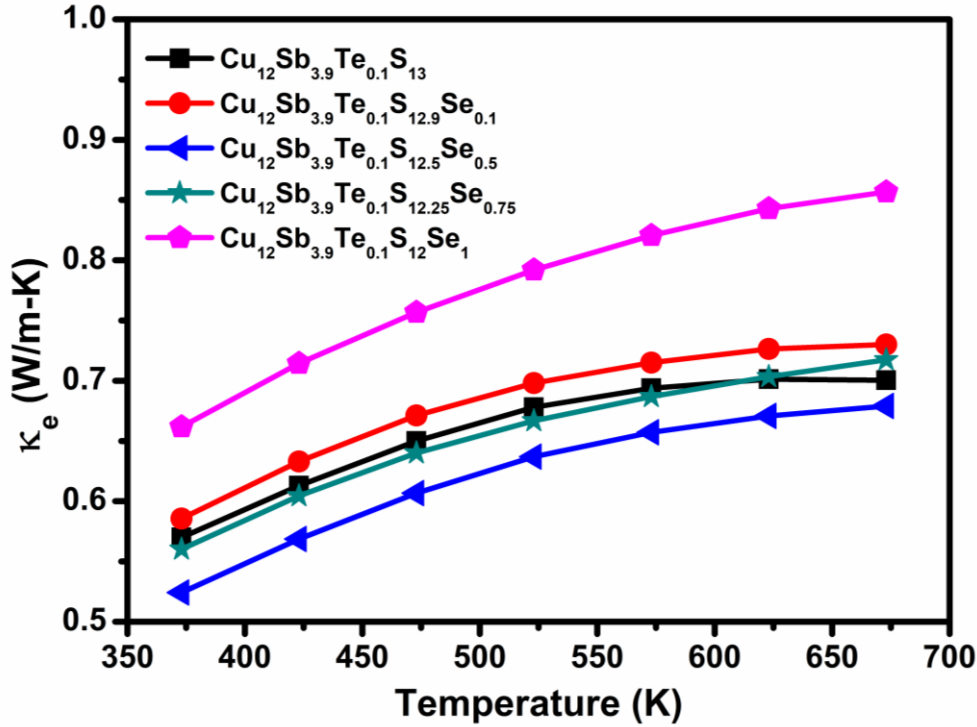


Fig. S10. Electronic thermal conductivity (κ_e) as a function of temperature of $\text{Cu}_{12}\text{Sb}_{3.9}\text{Te}_{0.1}\text{S}_{13-x}\text{Se}_x$ ($x = 0, 0.1, 0.5, 0.75$ and 1) samples.

References

- [1] P. Giannozzi, S. Baroni, N. Bonini, M. Calandra, R. Car, C. Cavazzoni, D. Ceresoli, G.L. Chiarotti, M. Cococcioni, I. Dabo, A. Dal Corso, S. De Gironcoli, S. Fabris, G. Fratesi, R. Gebauer, U. Gerstmann, C. Gougoussis, A. Kokalj, M. Lazzeri, L. Martin-Samos, N. Marzari, F. Mauri, R. Mazzarello, S. Paolini, A. Pasquarello, L. Paulatto, C. Sbraccia, S. Scandolo, G. Sclauzero, A.P. Seitsonen, A. Smogunov, P. Umari, R.M. Wentzcovitch, *J. Phys. Condens. Matter* 21 (2009) 395502.
- [2] J.P. Perdew, K. Burke, M. Ernzerhof, *Phys. Rev. Lett.* 77 (1996) 3865–3868.
- [3] Y. Bouyrie, C. Candolfi, V. Ohorodniichuk, B. Malaman, A. Dauscher, J. Tobola, B. Lenoir, *J. Mater. Chem. C* 3 (2015) 10476–10487.
- [4] S. Tippireddy, S. Ghosh, R. Biswas, T. Dasgupta, G. Rogl, P. Rogl, E. Bauer, R.C. Mallik, *J. Appl. Phys.* 127 (2020) 043712.
- [5] S. Tippireddy, R. Chetty, M.H. Naik, M. Jain, K. Chattopadhyay, R.C. Mallik, *J. Phys. Chem. C* 122 (2018) 8735–8749.
- [6] T. Barbier, P. Lemoine, S. Gascoin, O.I. Lebedev, A. Kaltzoglou, P. Vaqueiro, A. V. Powell, R.I. Smith, E. Guilmeau, *J. Alloys Compd.* 634 (2015) 253–262.
- [7] R. Chetty, A. Bali, M.H. Naik, G. Rogl, P. Rogl, M. Jain, S. Suwas, R.C. Mallik, *Acta Mater.* 100 (2015) 266–274.

- [8] X. Lu, D. Morelli, *J. Electron. Mater.* 43 (2014) 1983–1987.
- [9] X. Lu, D.T. Morelli, Y. Wang, W. Lai, Y. Xia, V. Ozolins, *Chem. Mater.* 28 (2016) 1781–1786.
- [10] S. Tippireddy, R. Chetty, K.K. Raut, M.H. Naik, P.K. Mukharjee, M. Jain, R. Nath, K. Wojciechowski, R.C. Mallik, *Phys. Chem. Chem. Phys.* 20 (2018) 28667–28677.
- [11] T. Wada, T. Maeda, *Phys. Status Solidi C* 14 (2017) 1600196.
- [12] L.I. Soliman, A.M. Abo El Soad, H.A. Zayed, S.A. El Ghfar, *Fizika. A* 11 (2002) 139–152.
- [13] H. Salehi, P. Amiri, R.Z. Hasanabad, *J. Optoelec. Nanostruc.* 3 (2017) 53-64.
- [14] S. Tippireddy, D.S. Prem Kumar, A. Karati, A. Ramakrishnan, S. Sarkar, S.C. Peter, P. Malar, K.H. Chen, B.S. Murty, R.C. Mallik, *ACS Appl. Mater. Interfaces* 11 (2019) 21686–21696.
- [15] X. Lu, W. Yao, G. Wang, X. Zhou, D. Morelli, Y. Zhang, H. Chi, S. Hui, C. Uher, *J. Mater. Chem. A* 4 (2016) 17096–17103.
- [16] B. Du, R. Zhang, K. Chen, A. Mahajan, M.J. Reece, *J. Mater. Chem. A* 5 (2017) 3249–3259.